Shapes, contact angles, and line tensions of droplets on cylinders

C. Bauer and S. Dietrich

Fachbereich Physik, Bergische Universität Wuppertal, D-42097 Wuppertal, Germany

(Received 28 February 2000)

Using an interface displacement model we calculate the shapes of nanometer-size liquid droplets on homogeneous cylindrical surfaces. We determine effective contact angles and line tensions, the latter defined as excess free energies per unit length associated with the two contact lines at the ends of the droplet. The dependences of these quantities on the cylinder radius and on the volume of the droplets are analyzed.

PACS number(s): 68.45.Gd, 68.10.−m, 82.65.Dp

I. INTRODUCTION

The wetting properties of a fiber in liquid matrices (e.g., dye mixtures, polymer melts, or molten resins) play an important role in the textile industry and in the fabrication of high-performance, fiber-reinforced composite materials. Since contact angles of liquid droplets on solid substrates provide a valuable characterization of such wetting properties there are numerous experimental and theoretical studies of the shape and the spreading of droplets deposited on a cylindrical substrate (see, e.g., Refs. [1–15]). The morphology of liquid drops on a fiber is particularly interesting insofar as on a planar substrate there is only one, spherical cap-like droplet shape, whereas on a cylindrical substrate droplets may exhibit two, topologically different shapes, a ''clamshell'' and a ''barrel'' shape, depending on the droplet volume, the contact angle, and the cylinder radius [1–3]. In the former case the droplet adheres to one side of the cylinder and exhibits a shape comparable with the shell of a mussel or clam or the armor of a tortoise, whereas in the latter case it surrounds the cylinder axisymmetrically, shaped like a barrel or a bale of thread wound up on a spindle. The aforementioned studies deal with thick fibers and large drops, i.e., the length scales are μm and larger. In this range the fluid structures are determined by macroscopic properties alone, i.e., volume of the liquid, surface tension σ of the liquid vapor interface, Young's contact angle θ_∞, and radius R of the cylinder.

However, with the discovery of nanotubes the interest in such fluid structures has shifted to much smaller scales. There are several applications for which these small solid–fluid structures are very important. (i) For fabricating valuable composite materials involving nanotubes their wetting by the liquid host matrix is necessary to couple the inherent strength of the nanotubes to the matrix, reinforcing materials or fillers for plastics and ceramics [16]. (ii) Nanotubes can be used as supports for heterogeneous catalysis or as templates for creating small wires or tubular structures by coating them with metals or metal oxides in the liquid state [17] or by attaching inorganic and organic moieties to the nanotube surfaces [18]. (iii) In order to use nanotubes as ''nanostraws'' potential candidates for exploiting such capillarity must be screened by first seeing if the liquid wets the *outside* of nanotubes [19]. The performance of the nanotubes as catalysts, adsorbants, and deodorants can vary depending on whether they are composed of carbon, boron nitride, or oxides

$(SiO_2, Al_2O_3, V_2O_5, MoO_3, TiO_2)$ [20]. This variety demonstrates that the substrate potential of these tubes can be regarded as a tunable parameter. (iv) By using nanotubes as nanotweezers [21] it might be possible to grab and manipulate small liquid drops. For this application the substrate must be nonwettable.

These small scales are comparable with the range of the substrate potential of the cylinders and of the molecular forces between the fluid particles adsorbing on them. Thus the droplets form under the action of the so-called effective interface potential ω, which accounts for the net effect of the competition between the forces among the fluid particles and the substrate potential [22]. Accordingly the calculation of the corresponding deformed droplet shapes requires a more detailed theoretical description which takes the effective interface potential into account. To our knowledge there is only one, recent publication in which this effect of ω on the droplet shape on fibers has been analyzed [23]. It is the purpose of our study here to refine and to extend this analysis in various directions. If the radius R of the fiber reduces to a few nm, as it is the case for nanotubes, the effective interface potential itself will depend on R and thus deviate from that of the corresponding semi-infinite planar substrate used in Ref. [23]. Accordingly we present a systematic analysis of the dependence of the shape of the droplets and their suitably defined contact angles on both R and the droplet volume. This enables us to describe systematically the crossover in shape and contact angle between those of droplets on a cylinder and on the limiting case $R \to \infty$ of a planar substrate. We remark on how the structure of the effective interface potential, depending on whether it leads to first-order or continuous wetting transitions, influences the morphology of the droplets. We confine our analysis to barrel-type droplets and estimate their metastability against roll-up to the clamshell configuration. Finally we study two types of line tensions. The first one concerns the line tension of three-phase contact between liquid, vapor, and substrate emerging at the ends of macroscopically large drops on fibers which reduces to the familiar line tension of the straight three-phase contact line on a planar substrate. The second excess free energy concerns the effective line tension associated with the circular shape of the three-phase contact line on a planar substrate as a function of the droplet volume. These results are relevant for understanding how to extract line tensions from contact angle measurements.
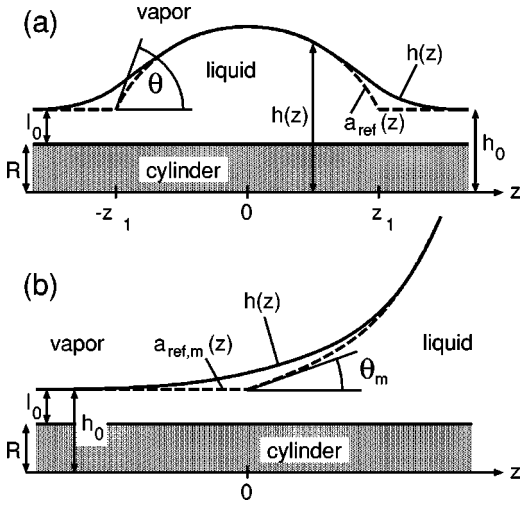
We are encouraged to present our refined analyses by re-

FIG. 1. (a) Schematic longitudinal cross section through a liquid droplet residing on a homogeneous cylindrical substrate with radius R. The system is rotationally symmetric around the z axis and symmetric with respect to a reflection at the plane $z=0$. $h(z)$ (full line) describes the liquid–vapor interface profile; the thickness of the liquid layer is $l(z)=h(z)-R$. The droplet shape is determined by the balance of the Laplace, the capillary, and the disjoining pressure [Eq. (2.8)]. Far from the droplet center, i.e., in the limit $|z| \to \infty$, the profile $h(z)$ reduces to a homogeneous layer $h(|z| \to \infty)=h_0$. $a_{\rm ref}(z)$ (dashed line) describes the reference surface which consists of a surface $a_{\rm ref}(|z| \leqslant z_1)=a(z)$ with constant mean curvature and of the homogeneous layer $a_{\rm ref}(|z| \geqslant z_1)=h_0$. $a(z)$ is determined by $a(z=0)=h(z=0)$ [i.e., it touches the actual surface profile $h(z)$ at the apex] and by the condition that the two principal radii of curvature $h(0)$ and R_0 [which is the radius of curvature of the planar curve $[z,h(z)]$, see Eq. (2.2)] of the actual and the reference surface at the apex are identical. The break in the slope of $a_{\rm ref}(z)$ at $z=\pm z_1$ defines the apparent contact angle θ. (b) Same as in (a), but for a macroscopic drop, i.e., infinite excess volume $V_{\rm ex}$. Choosing the position of one of the contact lines as the origin $z=0$ leads to a configuration for which the cylinder is in contact with bulk vapor for $z \to -\infty$ and with bulk liquid for $z \to \infty$. $a_{{\rm ref},m}(z \to \infty)$ and $h(z \to \infty)$ diverge exponentially. θ_m is defined by the break in the slope of $a_{{\rm ref},m}(z)$ at $z=0$.

cent experimental advances to determine droplet shapes such as microscopic interferometry [24], ellipsometric microscopy [25], scanning polarization force microscopy [26], and tapping-mode scanning force microscopy [27]. These techniques allow one to resolve drop profiles on the submicrometer scale [25,26] down to the nanometer scale [27], both vertically and laterally. In view of the numerous important applications mentioned above it would be rather rewarding to extend the application of these techniques to nonplanar substrate geometries in order to resolve experimentally the shape of droplets on fibers and tubes as presented in the following sections.

II. THEORY

A. Free energy functional

In cylindrical coordinates the droplet surface is described by a function $h(z)$ or $l(z)$ of the coordinate z along the symmetry axis of the cylinder [Fig. 1(a)]. We define $h(z)$ and $l(z)$ such that $h(z)$ is the local separation between the

liquid–vapor interface and the symmetry axis of the cylinder and $l(z)=h(z)-R$ is the local separation between the cylinder surface and the liquid–vapor interface, i.e., the liquid layer thickness. The droplet is also symmetric with respect to a reflection at the plane $z=0$. For large values of $|z|$, i.e., at large distances from the droplet center at $z=0$, the liquid forms a thin wetting layer of thickness $l_0=h_0-R$ around the cylinder. For reasons of simplicity $h(z)$ is henceforth assumed to be a unique function of z, i.e., we do not consider contact angles $\theta > 90°$. The shape of the liquid–vapor interface enclosing the droplet is determined by the interplay of three physical quantitites: the Laplace pressure [28] $2\sigma H$ generated by the mean curvature H of the interface with surface tension σ, the capillary pressure [28] induced by the finite droplet volume, and the disjoining pressure or, equivalently, the effective interface potential ω_c acting on the liquid–vapor interface [22]; $\omega_c(l;R)$ is the cost in free energy per surface area to maintain a homogeneous wetting layer of prescribed thickness l covering the cylinder surface and can be expressed in terms of the underlying forces of the substrate and between the fluid particles [29]. In the absence of the effective interface potential, i.e., for large droplets the liquid–vapor interface is a minimal surface under the constraint of a prescribed volume, i.e., it exhibits a constant mean curvature. The influence of the effective interface potential is most pronounced near the cylinder surface within the range of the substrate potential and leads to a deviation of the actual profile $h(z)$ from the shape which is determined by the aforementioned constant mean curvature condition. On the other hand, in the limit of large separation from the cylinder surface the mean curvature is asymptotically constant because there the influence of the effective interface potential vanishes.

Independent of the size of the droplet, for later purposes we define the "reference configuration" [see Fig. 1(a)]

$$a_{\rm ref}(z)=a(z)\Theta(z_1-|z|)+h_0\Theta(|z|-z_1), \quad (2.1)$$

where $a(z)$ is that constant-mean-curvature surface that touches the surface $h(z)$, $h(z=0)=a(z=0)$, and exhibits the same curvature H at the apex, i.e., the two principal radii of curvature

$$R_0=\frac{\{1+[h'(0)]^2\}^{3/2}}{h''(0)}=\frac{1}{h''(0)} \quad \text{with} \quad h' \equiv \frac{dh}{dz} \quad (2.2)$$

and $h(0)=R+l(0)$ of $h(z)$ and, correspondingly, of $a(z)$ [see Fig. 1(a)] at the apex position $z=0$ are identical. Θ denotes the Heaviside step function; $\pm z_1$ are those values of z where $a(z)$ and the homogeneous wetting layer $h(z) \equiv h_0$ intersect. In this sense the values $z=\pm z_1$ define the positions of the two three-phase contact lines forming the ends of the droplet. The "apparent contact angle" θ is defined by the intersection of the barrel-shaped part $a(z)$ of the reference profile and the homogeneous wetting layer $h(z) \equiv h_0$ [see Fig. 1(a)]:

$$\theta = \lim_{z \nearrow z_1} \arctan(|a'(z)|). \quad (2.3)$$

This apparent contact angle θ can be expressed [1,2] in terms of the measurable quantities apex height $l(0)$ of the droplet,

radius R of the cylinder, radius $R+l_0$ of the wetting film, and radius of curvature R_0 [Eq. (2.2)] of the profile $h(z)$ at the apex

$$\cos\theta = \frac{R+l(0)}{R+l_0} - \frac{[R+l(0)]^2-(R+l_0)^2}{2(R+l_0)}\left(\frac{1}{R+l(0)} + \frac{1}{R_0}\right).$$
(2.4)

Within an interface displacement model (see, e.g., Ref. [30]) the equilibrium interface configuration $\bar{h}(z)$ for a droplet of prescribed *excess* volume V_{ex} minimizes the free energy functional

$$F_{ex}[h(z)] = F[h(z)] - F[h_0]$$

$$= 2\pi\int_{-\infty}^{\infty}dz\{\sigma[h(z)\sqrt{1+h'(z)^2}-h_0]$$

$$+ R[\omega_c(h(z)-R)-\omega_c(h_0-R)]\}$$
(2.5)

under the constraint

$$\pi\int_{-\infty}^{\infty}dz[h^2(z)-h_0^2] = V_{ex}$$
(2.6)

and the boundary conditions $h(|z|\to\infty) = h_0$. We have defined $F_{ex}[h(z)]$ as an excess free energy with respect to the free energy $F[h_0]$ of the homogeneous wetting layer $h(z) \equiv h_0$ rendering a mathematically well-defined, finite expression. The first contribution to F_{ex} is the excess free energy due to the increase of the liquid–vapor interface as compared with a homogeneous cylindrical shape. In general σ itself depends on the curvature and thus on R (see, e.g., Sec. 2.2 in Ref. [29] and references therein); in the following, however, we do not discuss explicitly this additional parametric dependence on R. The second contribution to F_{ex} is the free energy generated by the effective interaction between the cylinder surface and the liquid–vapor interface, reduced by the corresponding free energy for the homogeneous wetting layer. Since the substrate is considered to be homogeneous, $\omega_c(l)$ depends only on the radial distance $l = h-R$ from the substrate surface. The equilibrium separation $h_0 = l_0+R$ of the homogeneous wetting layer from the cylinder axis minimizes the free energy $F(h) = 2\pi L[R\omega_c(h-R)+\sigma h]$ where $L \gg z_1$ is the macroscopic length of the cylinder. The constrained minimum of Eq. (2.5) is given by the unconstrained minimum of the surrogate functional

$$\mathcal{F}_{ex}[h(z)] = F_{ex}[h(z)] + \kappa\left(\pi\int_{-\infty}^{\infty}dz[h^2(z)-h_0^2] - V_{ex}\right).$$
(2.7)

The corresponding optimal profile $\tilde{h}(z,\kappa)$ renders the equilibrium profile $\bar{h}(z,V_{ex}) = \tilde{h}(z,\kappa(V_{ex}))$ upon expressing the Lagrange multiplier κ in terms of V_{ex} by inserting $\tilde{h}(z,\kappa)$ into the left hand side of Eq. (2.6) which yields the implicit relation $V_{ex}(\kappa)$. In order to avoid a clumsy notation, in the following we denote $\bar{h}(z,V_{ex})$ by $h(z)$. The Euler–Lagrange equation corresponding to Eq. (2.7) reads

$$\sigma\left(\frac{1}{h(z)[1+h'(z)^2]^{1/2}} - \frac{h''(z)}{[1+h'(z)^2]^{3/2}}\right)$$

$$= 2\sigma H(z) = -\kappa - \frac{R}{h(z)}\frac{d\omega_c(h-R)}{dh}\bigg|_{h=h(z)}.$$
(2.8)

This equation describes the balance between the Laplace pressure on the left hand side and the capillary plus disjoining pressure on the right hand side. One has $\kappa<0$ for any barrel-shaped droplet.

B. Reference profiles

The reference profile $a(z)$ minimizes a similar surrogate functional:

$$\mathcal{A}[a(z)] = \pi\int_{-z_1}^{z_1}dz[2\sigma a(z)\sqrt{1+a'(z)^2}+\kappa^*a^2(z)]+\text{const}$$
(2.9)

with the constant independent of $a(z)$ and the boundary conditions $a(\pm z_1) = h_0$. Equation (2.9) follows from Eq. (2.7) by omitting ω_c and replacing κ by κ^*. The corresponding Euler–Lagrange equation describes the constant-mean-curvature surface given by

$$\sigma\left(\frac{1}{a(z)[1+a'(z)^2]^{1/2}} - \frac{a''(z)}{[1+a'(z)^2]^{3/2}}\right) = 2\sigma H(z) = -\kappa^*.$$
(2.10)

According to the definition of $a(z)$ the Lagrange multiplier $-\kappa^*$ has to be chosen such that this constant mean curvature of this surface equals the mean curvature at the apex of the actual surface $h(z) = l(z)+R$

$$-\frac{\kappa^*}{\sigma} = \frac{1}{R+l(0)} + \frac{1}{R_0},$$
(2.11)

where R_0 [see Eq. (2.2)] and $R+l(0)$ are the principal radii of curvature at the apex of the actual surface $h(z)$, determined by the former Lagrange multiplier $\kappa(V_{ex})$. The solution of Eq. (2.10) is given implicitly by

$$\int_{h_0}^{a(z)}dy\left[\left(\frac{\sigma}{\kappa^*}\right)^2\left(\frac{2y}{\mathcal{C}-y^2}\right)^2-1\right]^{-1/2} = z+z_1, \quad |z|\le z_1,$$
(2.12)

which fulfills the boundary condition $a(-z_1) = h_0$; this determines implicitly z_1 in terms of h_0, V_{ex}, σ, and ω_c. The integration constant $\mathcal{C}$ is determined by $a'(0) = 0$ due to the symmetry of $a(z)$. The integral in Eq. (2.12) can be expressed in terms of elliptic integrals [31,32].

When the drop is macroscopically large ($V_{ex} = \infty$) it is appropriate to adopt a slightly different point of view. In this case not the center of the droplet but the position of one of the two three-phase contact lines, which are defined by the intersection of the asymptote $a_m(z)$ (the constant-mean-curvature surface appertaining to the *m*acroscopic drop) and $h(z) \equiv h_0$, is fixed at $z = 0$ [see Fig. 1(b)]. The actual inter-

face profile interpolates between, e.g., $h(z\to-\infty)=h_0$ and $h(z\to\infty)=a_m(z)$. This configuration describes a solid cylinder which is in contact with bulk vapor on the left hand side ($z\to-\infty$) and with bulk liquid on the right hand side ($z\to\infty$). The analysis of the internal structure of a three-phase contact line on a homogeneous, planar substrate is based on a similar configuration (see Refs. [33] and [34] and references therein). The interface profile diverges in the limit $z\to\infty$: $h(z\to\infty)\to\infty$, but this divergence is not linear as in the case of the planar substrate. A macroscopically large drop implies $\kappa\to0$. In this limit the volume constraint loses its meaning. Instead the state of the system is fixed by different lateral boundary conditions. In this case the solution of Eq. (2.12) is given by

$$a_m(z)=a(z;\kappa=0)=C\cosh\left(\frac{z-D}{C}\right) \qquad (2.13)$$

with two integration constants C and D. $a_m(z)$ describes a rotational surface with minimal surface area. From Eq. (2.13) one can easily see that the divergence of the interface profile for macroscopic drops is *exponential*, $a_m(z\to\infty)=(C/2)\exp[(z-D)/C]$, rather than linear as on a planar substrate. The reference profile appertaining to the macroscopic drop is

$$a_{\text{ref},m}(z)=a_m(z)\Theta(z)+h_0\Theta(-z). \qquad (2.14)$$

The slopes at the intersection of the asymptote $a_m(z)$ and the homogeneous layer $h(z)\equiv h_0$ at $z=0$ defines the contact angle $\theta_m(R)=\theta(R,V_{\text{ex}}\to\infty)$. $R=\infty$ corresponds to a planar substrate for which the interface profile diverges *linearly* in the limit $z\to\infty$

$$a_{m,\infty}(z)-R=l_0+z\tan\theta_\infty \qquad (2.15)$$

with the macroscopic contact angle $\theta_\infty=\theta_m(R\to\infty)$ on the planar substrate. θ_∞ obeys Young's law $\cos\theta_\infty=(\sigma_{\text{wg}}-\sigma_{\text{wl}})/\sigma$, where σ_{wg} and σ_{wl} are the wall–gas and wall–liquid surface tensions, respectively; $\sigma_{\text{wg}}-\sigma_{\text{wl}}=\omega_c(l_0;R=\infty)$ is determined by the effective interface potential of the corresponding planar substrate (see, c.f., Sec. II C). On the cylindrical surface the contact angle $\theta_m(R)$ does not follow from similar thermodynamic considerations but follows from the numerical analysis of the full profile $h(z)$ for large V_{ex} (see, c.f., Sec. III and Fig. 9).

The integration constants C and D in Eq. (2.13) can be determined from the conditions $a_m(z=0)=R+l_0$ and $a'(z=0)=\tan\theta_m$ so that

$$a_m(z)=R\cos\theta_m\cosh\left(\frac{z}{R\cos\theta_m}+\text{arccosh}\frac{1}{\cos\theta_m}\right). \qquad (2.16)$$

The series expansion of this expression in terms of small z/R is

$$a_m(z/R\ll1)=R+l_0+z\tan\theta_m(R)+\mathcal{O}(z^2). \qquad (2.17)$$

In the limit $R\to\infty$ the region where the higher order terms are relevant is shifted towards $z=\infty$ such that, with $\theta_m(R\to\infty)=\theta_\infty$, one recovers the linearly diverging asymptote $a_{m,\infty}(z)$ [Eq. (2.15)].

C. Effective interface potential

For the same liquid layer thickness l the effective interface potential $\omega_c(l;R)$ of a cylinder differs from that of a planar substrate $\omega_p(l)$. The full expression $\omega_c(l;R)$ is presented in Ref. [29] as obtained from density functional theory and within a so-called sharp-kink approximation for the solid–liquid and the liquid–vapor interface profiles. For reasons of simplicity, here we use the leading order of a series expansion of $\omega_c(l;R)$ in terms of d_w/R, where d_w is the radial extension of the volume excluded for the fluid particles due to the repulsive part of the substrate potential

$$\omega_c(l;R)=\frac{3\pi}{2}a\frac{R}{h^3}{}_2F_1\left[\frac{5}{2},\frac{3}{2};2;\left(\frac{R}{h}\right)^2\right]$$
$$+8b\frac{R}{h^4}{}_2F_1\left[3,2;2;\left(\frac{R}{h}\right)^2\right]$$
$$+\frac{315\pi}{32}c\frac{R}{h^9}{}_2F_1\left[\frac{11}{2},\frac{9}{2};2;\left(\frac{R}{h}\right)^2\right]+\mathcal{O}\left(\frac{d_w}{R}\right), \qquad (2.18)$$

with $h=l+R$ and ${}_2F_1$ hypergeometric functions. In the limit $l/R\to0$ one recovers the expression for the effective interface potential of the corresponding planar substrate

$$\omega_c(l;R\to\infty)=\omega_c(l\to0,R)=\omega_p(l)=al^{-2}+bl^{-3}+cl^{-8}. \qquad (2.19)$$

However, the power-law decay of $\omega_c(l\to\infty)$ for a fixed, finite cylinder radius R is

$$\omega_c(l\to\infty;R)=\frac{3\pi}{2}a\frac{R}{l^3}+O(l^{-4}), \qquad (2.20)$$

i.e., one power faster than that for the corresponding planar substrate.

At present there exists, to our knowledge, only one study concerned with the shapes of droplets on cylinders within the range of the effective interface potential between the cylinder surface and the liquid–vapor interface [23]. However, in Ref. [23] the *disjoining pressure* $\Pi_c(l)=-[R/(R+l)]d\omega_c(l)/dl$ on the right hand side of the Euler–Lagrange equation (2.8) as a whole rather than only the effective interface potential ω_c is replaced by the disjoining pressure of the corresponding planar substrate $\Pi_p(l)=-d\omega_p(l)/dl$. In view of Eqs. (2.19) and (2.20), except for the factor $R/(R+l)$, this corresponds to the short-distance expansion ($l/R\to0$) of the effective interface potential of the cylinder. This replacement of the disjoining pressure by that of the planar substrate is expected to yield numerically reliable results only for large cylinder radii and small liquid layer thick-

nesses $l \ll R$. Therefore in Sec. III we test the quality of this approximation (as well as that of the replacement of ω_c alone by ω_p).

So far, due to the volume constraint, our considerations apply to nonvolatile liquids. For volatile liquids any droplet surrounded by a macroscopic reservoir of vapor phase is thermodynamically unstable against evaporation, leaving behind only the thin equilibrium wetting film. However, we expect that the actual nonequilibrium state of a condensating or evaporating liquid observed within a time scale that is small compared with the typical condensation or evaporation time can be described by solutions of Eq. (2.8) with V_{ex} given by its momentary value. Only the interface configuration for $\kappa = 0$, i.e., $V_{ex} = \infty$, which interpolates between a homogeneous wetting layer and an exponentially diverging profile, describes a bona fide thermodynamically stable state which can be maintained by imposing appropriate boundary conditions (see above) at liquid–vapor coexistence for the bulk fluid. The thermodynamic state, which in a grand canonical ensemble is defined by temperature and chemical potential, enters parametrically into the actual values of the effective interface potential ω_c and the liquid–vapor surface tension σ.

III. SHAPES OF DROPLET SURFACES AND CONTACT ANGLES

We solve the Euler–Lagrange equation (2.8) numerically for fixed values of κ and for a given effective interface potential $\omega_c(l)$; the value of κ, in turn, determines the excess liquid volume V_{ex} and allows us to establish the relation $\kappa(V_{ex})$. As boundary conditions in the case $\kappa < 0$ (leading to droplets of finite size) we use that $h(z)$ must approach the wetting layer thickness h_0 for large z and that $h'(z=0)=0$. The distance $L/2$, at which the system is cut off, is chosen large enough so that $h(z=L/2)$ and $h'(z=L/2)$ attain their asymptotic values h_0 and 0, respectively, within prescribed accuracy. The reference profile $a_{ref}(z)$ is then calculated numerically by solving the differential equation (2.10) with κ^* determined by Eqs. (2.2) and (2.10) and with $a(z=0)=h(z=0)$ and $a'(z=0)=0$, up to the point of intersection of $a(z)$ and h_0 which defines the coordinate z_1; $a_{ref}(z \geq z_1)=h_0$. The contact angle θ is determined from Eq. (2.3) and, as a crosscheck, from Eq. (2.4).

In all numerical calculations presented henceforth we set $a=3\sigma s^2$, $b=-5\sigma s^3$, and $c=3\sigma s^8$ such that s sets the length scale for the range of the effective interface potential (typically $s \approx 1$ nm). We divide both sides of Eq. (2.8) by σ so that $\omega(l)/\sigma$ is dimensionless and κ/σ has the dimension of an inverse length. Alternatively, instead of introducing s as above one can choose $\sqrt{a/\sigma}$ as the basic length scale which describes the decay of the effective interface potential; for our choice $\sqrt{a/\sigma} \approx 1.73s$. The effective interface potentials $\omega_c(l;R)$ [Eq. (2.18)] and $\omega_p(l)$ [Eq. (2.19)] for the above choice of coefficients are shown in Fig. 2.

As a first example we solve Eq. (2.8) with the effective interface potential $\omega_p(l)$ of the corresponding planar substrate [Eq. (2.19)] and the potential coefficients given above. Figure 3 shows the profile of the droplet surface on a cylinder with radius $R=100s$ for $\kappa s/\sigma = -0.1$. This choice of κ leads to a small droplet with $V_{ex} \approx 1.46 \times 10^4 s^3$ (i.e., con-
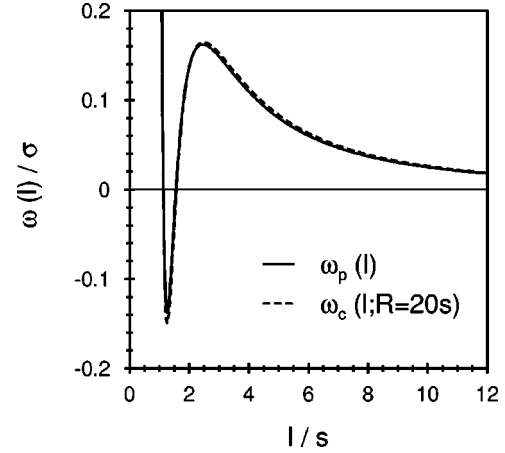

FIG. 2. Model effective interface potentials $\omega(l)$ in units of the planar liquid–vapor surface tension σ as used in all numerical calculations. $\omega_c(l;R)$ and $\omega_p(l)$ are given by Eqs. (2.18) and (2.19), respectively, with $a/\sigma = 3s^2$, $b/\sigma = -5s^3$, and $c/\sigma = 3s^8$, where s sets the length scale of the system (typically $s \approx 1$ nm). The full line denotes the effective interface potential $\omega_p(l)$ for the planar substrate, the dashed line denotes $\omega_c(l;R)$ for a cylinder with $R = 20s$. For this choice of parameters and within the range of values of l shown here the effective interface potentials even of thin cylinders barely differ from that of a planar substrate. Only for large l the long-range decay of $\omega_p(l)$ and $\omega_c(l)$ differ qualitatively [compare Eq. (2.20)]. This type of effective interface potential with a global minimum at $l_0/s \approx 1.3$ and a second, local minimum at $l = \infty$ leads to a first-order wetting transition of a planar substrate at a higher wetting transition temperature at which the first minimum raises up to $\omega = 0$. In the case of a continuous wetting transition $\omega(l)$ would exhibit a single minimum and approach $\omega = 0$ from below in the absence of a potential barrier in between.
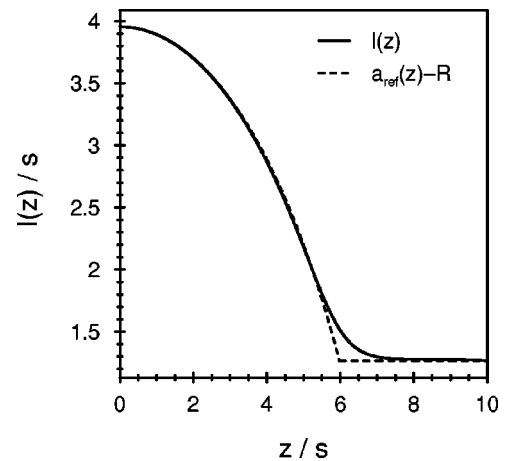

FIG. 3. Profile $l(z)$ of the droplet surface (full line) and the corresponding reference profile $a_{ref}(z)-R$ (dashed line) for $R = 100s$, $\kappa s/\sigma = -0.1$ so that $V_{ex} \approx 1.46 \times 10^4 s^3$, and the effective interface potential $\omega_p(l)$ of the corresponding planar substrate as shown in Fig. 2. The droplet is so small that its liquid–vapor interface lies entirely within the range of $\omega_p(l)$. For $z/s \gtrsim 5.25$ the interface profile $l(z)$ lies above the reference profile $a(z)-R$ and, for $z/s \lesssim 5.25$ upon approaching the apex of the droplet, it reaches the reference profile from below. This particular droplet is possibly metastable against the ''rollup'' to the ''clamshell'' shape because the stability criterion Eq. (3.1) is not satisfied.
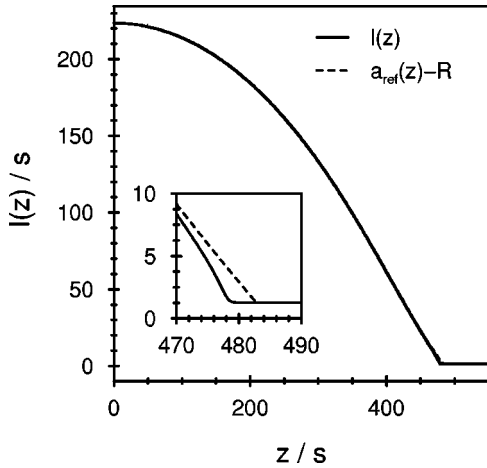
FIG. 4. Profile $l(z)$ of the droplet surface (full line) and the corresponding reference profile $a_{ref}(z) - R$ (dashed line) for the same set of parameters as in Fig. 3, but with $\kappa s/\sigma = -0.005$ so that $V_{ex} \approx 1.67 \times 10^8 s^3$. In contrast to the situation shown in Fig. 3, here the droplet is so large that it extends up to distances from the cylinder surface where the effective interface potential is negligible. The inset magnifies the region around the three-phase contact line at $z = z_1 \approx 483s$. In the region around the apex of the droplet the profile $l(z)$ lies below the reference profile. Since the effective interface potential is the same as in Fig. 3 the absolute deviation of $h(z)$ from $a_{ref}(z)$ is about the same size as in Fig. 3 (see the inset). According to Eq. (3.1) this droplet is stable against ''rollup.''

taining roughly 10^7 fluid particles) whose liquid–vapor interface lies entirely within the range of the effective interface potential. Therefore the deviation of the profile from the asymptote $a(z)$ extends up to the apex of the droplet. The model effective interface potential used here resembles a typical interface potential leading to first-order wetting on a planar substrate [22]. The droplet surface crosses the reference profile and, upon approaching the apex of the droplet, it reaches the reference profile from below.

Carroll [2] has shown that, in the absence of the effective interface potential, the axisymmetric droplet configuration is only stable for

$$2 \left(\frac{h(0)}{R} \right)^3 \cos \theta - 3 \left(\frac{h(0)}{R} \right)^2 + 1 > 0, \qquad (3.1)$$

i.e., if the droplet is large compared with the diameter of the cylinder and if the contact angle is small. When the droplet volume decreases or the contact angle increases the axisymmetric droplet becomes metastable against a so-called ''rollup'' towards the ''clamshell'' configuration [35]. By applying the stability criterion Eq. (3.1) to the interface profile shown in Fig. 3, we find that this barrel-type configuration is possibly metastable towards forming the ''clamshell'' shape. A definitive statement about the stability would require us to refine the criterion in Eq. (3.1) by incorporating the effect of the effective interface potential. However, the determination of the nonaxisymmetric ''clamshell'' equilibrium shape requires a much larger numerical effort and is therefore beyond the scope of the present paper. One can define a critical value $V_{ex,c}$ such that for $V_{ex} > V_{ex,c}$ the axisymmetric droplet is stable. Upon increasing R, $V_{ex,c}$ increases, too; $V_{ex,c} \to \infty$ in the limit $R \to \infty$. Only for $V_{ex} = \infty$,
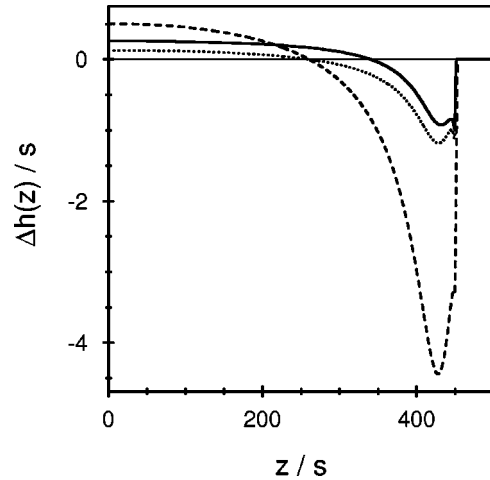

FIG. 5. Full line: difference $\Delta h(z) = h_c(z) - h_p(z)$ between the two droplet profiles h_c and h_p for $\kappa s/\sigma = -0.005$ [leading to a droplet with $l(0) \approx 361s$ and $z_1 \approx 453s$] and $R = 20\sigma$ which are calculated by using $\omega_c(l; R = 20s)$ and $\omega_p(l)$, respectively. For comparison, the dotted line shows the difference between the profile h_c for $R = 20s$ and $\kappa s/\sigma = -0.005$ and the profile $\tilde{h}_p$ for $R = 20s$, but with κ chosen such that the excess volumes of liquid for both profiles h_p and h_c are identical. In order to achieve this, for the determination of $\tilde{h}_p$ the value of $\kappa s/\sigma$ has to be increased by 1.63 $\times 10^{-6}$. In both cases the maximal difference is of the order of s. Since Δh changes sign as a function of z, it is not possible to find an effective value κ_{eff} such that for a given value of κ the resulting profile calculated with ω_p is identical with the profile h_c. The dashed line denotes the difference Δh between the profile $h_c(z)$ for $\kappa s/\sigma = -0.005$ and $R = 20s$ and the profile $\bar{h}_p(z)$ for which, as in Ref. [23], in Eq. (2.8) the entire disjoining pressure $[R/(R +l)]d\omega_c/dl$ (instead of only $d\omega_c/dl$) is replaced by the disjoining pressure of the planar substrate $d\omega_p/dl$; here for the determination of $\bar{h}_p$ the value of $\kappa s/\sigma$ has been increased by 6.58×10^{-6} in order to have identical excess liquid volumes. This approximation is worse than the substitution of the effective interface potential alone, although the difference Δh is still on the order of s.

i.e., for macroscopic drops, and for contact angles smaller than 90° (as stated in Sec. II here we do not consider the case $\theta > 90°$) the rotationally symmetric interface shape is stable for any value of R.

Figure 4 shows the droplet shape for the same choice of potential parameters and for the same cylinder with $R = 100s$, but for $\kappa s/\sigma = -0.005$. This choice of κ leads to a much bigger droplet with $V_{ex} \approx 1.67 \times 10^8 s^3$. The apex of the droplet is located at such a large distance from the cylinder surface that the effective interface potential is almost negligible. Therefore the application of Eq. (3.1) is reliable; it shows that this particular droplet is indeed stable against ''rollup.'' In the vicinity of the cylinder surface the absolute deviation of the interface profile from the asymptote is similar to that in Fig. 3. As compared with the situation shown in Fig. 3, the point where $l(z)$ crosses the reference profile $a(z) - R$ is shifted to the right and lies near the three-phase contact line at $z = z_1$. For the model effective interface potential used here and in Fig. 3, in the region around the apex of the droplet the profile lies below the reference profile. These results are in accordance with the findings for the planar, homogeneous substrate [33,34] with the same type of
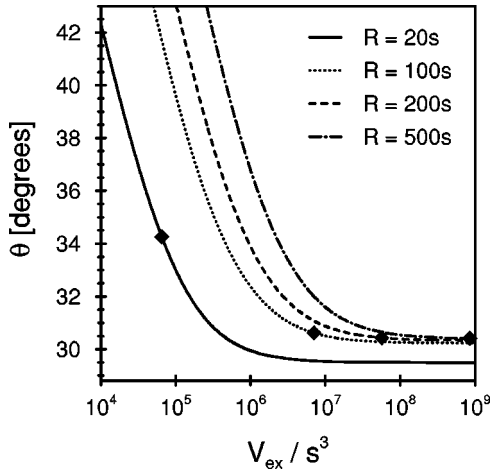
C. BAUER AND S. DIETRICH

PRE 62

FIG. 6. Apparent contact angles θ for the same effective interface potential $\omega_p(l)$ as used for Figs. 3 and 4 and for different cylinder radii R as a function of the liquid excess volume V_{ex}. The main effect of increasing R is a shift of the curves upwards and to the right. The limit $V_{ex} \to \infty$ corresponds to macroscopic drops or, equivalently, a cylinder in contact with bulk vapor at one end and with bulk liquid at the other [compare Fig. 1(b) and, c.f., Figs. 8 and 9]. The differences between the curves are minimal in the limit $V_{ex} \to \infty$. $\theta(V_{ex})$ is, for any value of R, a monotonously decreasing function with vanishing slope $d\theta/dV_{ex} = 0$ in the limit $V_{ex} \to \infty$. The symbols ◆ indicate the critical values $V_{ex,c}$ above which according to the criterion in Eq. (3.1) the axisymmetric droplet shape considered here is stable, but below which the "clamshell" configuration is stable.

interface potential. If, on the other hand, $\omega(l)$ corresponds to a system undergoing a continuous wetting transition, i.e., exhibiting a single minimum without a potential barrier, the profile of the droplet shape approaches its asymptote from the outside without crossing it (see Fig. 8 in Ref. [34]).

Figure 5 displays the effect of the replacement of the effective interface potential of a cylinder $\omega_c(l;R)$ [Eq. (2.18)] by that of the corresponding planar substrate $\omega_p(l)$ [Eq. (2.19)] for a droplet with $\kappa s/\sigma = -0.005$ so that $l(0) \approx 361s$ and $z_1 \approx 453s$ on a thin cylinder with $R = 20s$. This droplet also satisfies the stability criterion in Eq. (3.1). For reasons of clarity in this figure we have plotted the difference $\Delta h(z)$ between corresponding profiles instead of the profiles themselves. The influence of approximating $\omega_c(l;R)$ by $\omega_p(l)$ turns out to be rather small: the difference $\Delta h(z)$ is at most on the order of s. It is even smaller in the case of smaller droplets and thicker cylinders: the quality of approximating $\omega_c(l;R)$ by $\omega_p(l)$ improves if the cylinder is thicker and the droplet is smaller. In Ref. [23] the disjoining pressure of a cylinder rather than the effective interface potential is replaced by its planar-substrate counterpart. This corresponds to replacing the term $(R/h)d\omega_c/dl$ on the right hand side of Eq. (2.8) by $d\omega_p/dl$. The dashed line in Fig. 5 shows the effect of this approximation on the surface profile. As expected, the quality of this approximation is worse than the substitution of the effective interface potential alone, although the difference Δh is still of the order of s.

Figure 6 shows the apparent contact angles for the examples presented in Figs. 3 and 4, as well as for the same set of potential parameters but with $R = 20s$, $R = 200s$, and $R = 500s$ as function of the excess liquid volume V_{ex}. Upon
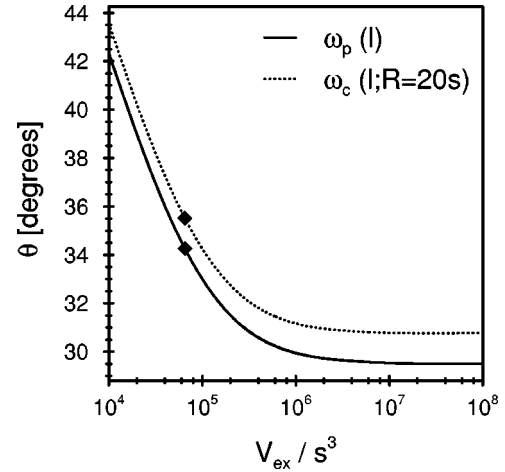

FIG. 7. Apparent contact angles θ calculated by using $\omega_c(l;R)$ (dotted line) as compared with those calculated based on $\omega_p(l)$ (full line) as a function of the excess liquid volume V_{ex} for a cylinder with $R = 20s$ (i.e., the full line is identical to the full line in Fig. 6). Both curves exhibit the same qualitative behavior. For thicker cylinders whose contact angles $\theta(V_{ex})$ are shown in Fig. 6 the differences between the curves are much smaller. The symbols ◆ indicate the critical values $V_{ex,c}$ above which the axisymmetric droplet shape considered here is stable, but below which the "clamshell" configuration is stable [compare Eq. (3.1)]. The difference between the two curves is largest for macroscopically large drops.

increasing R the curves are shifted upwards and to the right. Due to the exponential divergence of the interface profile of a macroscopic drop [which is more pronounced for smaller R, see the discussion of Eqs. (2.16) and (2.17) above and see Fig. 8], the determination of the apparent contact angles for very large drops is, in particular for thin cylinders, numerically difficult. However, the data indicate that, for any value of R, $\theta(V_{ex})$ is a monotonously decreasing function, with a vanishing slope $d\theta/dV_{ex} = 0$ at $V_{ex} = \infty$. The differences between the contact angles for different R are minimal at $V_{ex} = \infty$. For any R there is a sizeable increase of the apparent contact angle upon decreasing droplet size.

Figure 7 shows the effect of replacing ω_p by ω_c on the apparent contact angles for the system with $R = 20s$ (compare Fig. 5). The difference between the contact angles calculated by using ω_c and ω_p is significant. It is much smaller for thicker cylinders whose contact angles are displayed in Fig. 6. However, the qualitative functional form of the dependence of $\theta(V_{ex})$ is not affected by the replacement of ω_c by ω_p.

For macroscopic drops (i.e., $\kappa = 0$ or, equivalently, $V_{ex} = \infty$) the Euler–Lagrange equation is solved with the initial value $h(z = L_1) = h_0$ and a small initial slope $h'(z = L_1)$ [e.g., $h'(z = L_1) = 10^{-8}$]; the initial slope $h'(z = L_1) = 0$ would yield the trivial solution $h = h_0$. In order to find the asymptote we determine the integration constants C and D in Eq. (2.13) such that $a_m(L_2) = h(L_2)$ and $a'_m(L_2) = h'(L_2)$, where $z = L_2$ is the coordinate up to which the differential equation is integrated numerically; the system size $L_2 - L_1$ is chosen large enough so that upon further increase of the system size C and D remain unchanged within prescribed accuracy. The contact angle θ_m can be inferred from the value of C [Eq. (2.16)]. Finally the coordinate system is
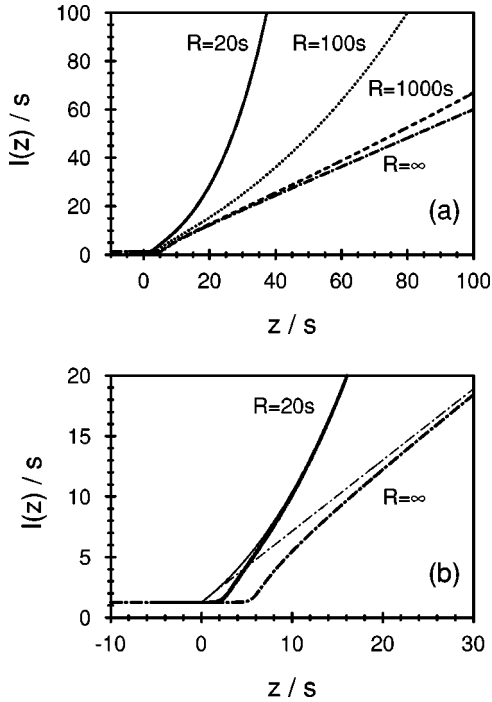
FIG. 8. (a) Liquid–vapor interface profiles $l(z)=h(z)-R$ of macroscopic drops ($V_{ex}=\infty$) for $R=20s$ (full line), $R=100s$ (dotted line), $R=1000s$ (dashed line), and $R=\infty$ (dashed-dotted line), calculated with $\omega_p(l)$. (b) The profiles $l(z)$ (thick lines) and their corresponding reference configurations $a_{ref}(z)-R$ (thin lines) for $R=20$ s and $R=\infty$ are shown in the magnified region around the contact line at $z=0$; here we use the same graphical notation as in (a). Each reference configuration consists of the horizontal line $l(z)=l_0$ for $z<0$ and of the asymptotic branch $a_m(z)-R$ for $z>0$; for $R<\infty$ this asymptote diverges exponentially in the limit $z\to\infty$ [see Eq. (2.16)]. $R=\infty$ corresponds to the planar substrate for which $a_{m,\infty}(z)$ is a *linear* function. As demonstrated in (a), in the limit $R\to\infty$ the region where higher-order corrections to the linearly diverging asymptote become relevant is progressively shifted towards $z\to\infty$, such that for $R=\infty$ only the linear divergence remains. The appertaining contact angles θ_m and the line tension τ as a function of R are shown in, c.f., Figs. 9 and 10, respectively. Since for macroscopic drops the contact angles attain a finite value, for any radius R the stability criterion in Eq. (3.1) for the barrel-type shape is fulfilled.

shifted laterally such that the intersection of $a_m(z)$ and h_0 define the position $z=0$ (which corresponds to $z=-z_1$ for $\kappa\neq0$). As mentioned before, for macroscopic drops the rotationally symmetric configuration satisfies the stability criterion Eq. (3.1) for any R.

The dependence of the liquid–vapor interface profiles of macroscopic drops on the cylinder radius R is shown in Fig. 8 using $\omega_p(l)$ and with the same set of interaction potential parameters as in the previous examples. In accordance with Eq. (2.16), the interface profiles for cylinders of finite thickness diverge exponentially in the limit $z\to\infty$. In the limit $R\to\infty$ the region where higher-order corrections to the linear behavior [Eq. (2.17)] are relevant is shifted towards $z\to\infty$ such that in the limiting case $R=\infty$ corresponding to the planar substrate the linear divergence of the reference profile is recovered. Figure 9(a) displays the apparent contact angles θ_m corresponding to the profiles shown in Fig. 8 as a function of R. Upon increasing the cylinder radius R, θ_m ap-
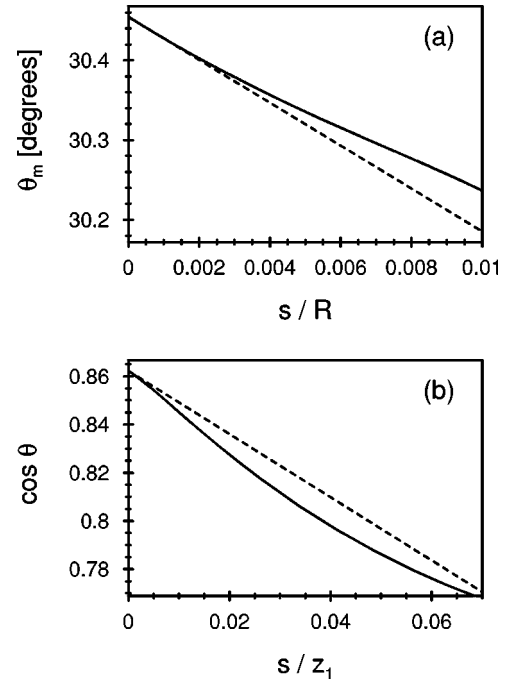

FIG. 9. (a) Apparent contact angles θ_m for *macroscopic* drops ($V_{ex}=\infty$) as a function of R (full line) corresponding to the interface profiles shown in Fig. 8. As indicated by the dashed line, in the limit $R\to\infty$ the apparent contact angles attain Young's contact angle $\theta_\infty\approx30.5°$ on the corresponding planar substrate as $\theta_\infty-\theta_m\sim R^{-1}$. (b) Apparent contact angle $\cos\theta$ of *small* droplets (full line) on the *planar* substrate as a function of the radius z_1 of the base of the spherical cap acting as the corresponding reference configuration. For large drops $\cos\theta$ varies according to the Neumann–Boruvka equation (dashed line) $\cos\theta-\cos\theta_\infty=-\tau_\infty/(\sigma z_1)$ which allows one to determine experimentally the line tension τ_∞ of three-phase contact on a planar substrate. Here $\tau_\infty=1.31\sigma s$. The deviation between the full line and the dashed line shows that the Neumann–Boruvka equation is applicable only for $z_1/s\gtrsim500$.

proaches Young's contact angle θ_∞ for the planar substrate as $\theta_\infty-\theta_m\sim R^{-1}$.

In Fig. 9(b) we show the apparent contact angles of *small* droplets on a *planar* substrate, i.e., in the limit $R\to\infty$ but with $V_{ex}<\infty$. In this case the reference configuration is a spherical cap whose circular base has a radius z_1 [see Fig. 1(a)]. For large droplets $\cos\theta$ reaches Young's contact angle $\cos\theta_\infty$ according to the Neumann–Boruvka equation [28,36]

$$\cos\theta-\cos\theta_\infty=-\frac{\tau_\infty}{\sigma z_1}, \qquad (3.2)$$

which allows one to determine experimentally the line tension τ_∞ of three-phase contact on a planar substrate by varying the droplet size. Figure 9(b) demonstrates that this linear relationship between $\cos\theta$ and z_1^{-1} is valid only for $z_1/s\gtrsim500$, i.e., for $z_1\gtrsim500$ nm. From Fig. 9(b) one infers that $\cos\theta$ decreases more rapidly than predicted by Eq. (3.2). This behavior can be accounted for by an effective line tension $\tau_{eff}(z_1)$ which due to the circular bending of the three-phase contact line is *larger* than the value τ_∞ of the corresponding *straight* three-phase contact line. Similar results have been obtained by Dobbs [37].

θ and θ_m depend on the liquid–vapor surface tension σ which in turn also exhibits a behavior $\sigma(R) - \sigma(\infty) \sim R^{-1}$. In accordance with the discussion in Sec. II A, Fig. 9 does not yet take into account this indirect dependence of θ and θ_m on R via $\sigma(R)$.

IV. LINE TENSION

As long as the size of a droplet is *finite* and *fixed* it is impossible to extract from the total free energy unambiguously and in a strict thermodynamic sense a line tension associated with the three-phase contact lines at the ends of the droplet because there are arbitrarily many ways to form the total free energy as a sum of various terms. However, *well-defined* line tensions emerge as coefficients in the *size dependence* of the free energy of droplets upon approaching macroscopic drops. To this end we consider the limit of large drops, i.e., $V_{ex}s^{-3} \gg 1$ and $z_1/s \gg 1$ [see Fig. 1(a)]. Within the interface displacement model the excess free energy in Eq. (2.5) can be rewritten as

$$F_{ex} = \sigma A_b - 4\pi R \omega_c(l_0) z_1 - \sigma A_c + \mathcal{L}, \qquad (4.1)$$

where

$$A_b = 2\pi \int_{-z_1}^{z_1} dz\, a_{ref}(z)\sqrt{1 + [a'_{ref}(z)]^2} \qquad (4.2)$$

is the surface area of the "barrel" part of the reference surface $a_{ref}(z)$, $-z_1 \leq z \leq z_1$, $A_c = 4\pi h_0 z_1$ is the surface area of the cylinder with radius h_0 and length z_1 [see Fig. 1(a)], and

$$\mathcal{L} = 2\pi \int_{-\infty}^{\infty} dz \{ \sigma[h(z)\sqrt{1 + [h'(z)]^2}$$
$$- a_{ref}(z)\sqrt{1 + [a'_{ref}(z)]^2}] + R[\omega(h(z) - R)$$
$$- \omega(a_{ref}(z) - R)]\} + 2\pi R \int_{-z_1}^{z_1} dz\, \omega(a_{ref}(z) - R). \tag{4.3}$$

For $V_{ex} \to \infty$, F_{ex} [Eq. (4.1)] is dominated by the term σA_b which scales proportional to the surface area of the drop and thus represents a two-dimensional contribution. The leading subdominant terms are $-4\pi R \omega_c(l_0) z_1$ and $-4\pi h_0 \sigma z_1$, which scale with the linear dimension $2z_1$ of the drop representing one-dimensional contributions. Finally, the last term in Eq. (4.1) remains finite for V_{ex}, A_b, and $z_1 \to \infty$

$$\mathcal{L}(z_1) = \mathcal{T} + \mathcal{O}(z_1^{-1}) \qquad (4.4)$$

and thus represents a zero-dimensional contribution. In its turn $\mathcal{T}$ depends on the cylinder radius R such that for large R it scales proportional to R, which leads to the following definition of an excess free energy per unit length, henceforth called "line tension," associated with the two contact lines formed at the ends of the droplet with total length $4\pi R$:

$$\tau = \frac{\mathcal{T}}{4\pi R}. \qquad (4.5)$$

We note that $\mathcal{T}$ is only well defined in the thermodynamic limit $\lim_{A_b, z_1 \to \infty} (F_{ex} - \sigma A_b + 4\pi R \omega_c(l_0) z_1 + \sigma A_c)$ so that higher order terms, e.g., $\sim z_1^{-1}$, omitted on the right hand side of Eq. (4.4), drop out. In the following $\mathcal{T}$ is understood to have been obtained via this procedure. It can be expressed in terms of the solution of Eq. (2.8) for $\kappa = 0$ and of $a_{ref,m}(z)$ [Eqs. (2.13) and (2.14)]

$$\mathcal{T} = 4\pi \int_{-\infty}^{\infty} dz \{ \sigma[h(z)\sqrt{1 + (h'(z))^2}$$
$$- a_{ref,m}(z)\sqrt{1 + [a'_{ref,m}(z)]^2}] + R\{\omega(h(z) - R)$$
$$- \omega(a_{ref,m}(z) - R)\} + 4\pi R \int_0^{\infty} dz\, \omega(a_{ref,m}(z) - R). \tag{4.6}$$

Consequently, $\mathcal{T}$ is twice the characteristic excess free energy associated with the structure of a macroscopic drop near one of its ends without interference from the other end. On the other hand, $\mathcal{T}$, and thus τ, are defined for any value of R. The ratio τ formed in Eq. (4.5) has the property that in the limit $R \to \infty$ it reduces to the line tension τ_∞ of the straight three-phase contact line on the corresponding planar substrate (see, e.g., Refs. [30,33,34,38]), which is an experimentally observable quantity [compare Fig. 9(b)].

At this stage one should note that the above considerations tacitly assume that another thermodynamic limit concerning the total system size, such as the volume of the surrounding vapor phase and the length L of the solid cylinder, has already been carried out in advance: $F(h_0)$ is proportional to L and has been subtracted before. Moreover, we have not considered the bulk free energy of the surrounding vapor phase and the bulk free energy of the liquid in the drop proportional to V_{ex} because they do not enter the description of the droplet shape in terms of an interface displacement model. As a careful analysis of the line tension τ_∞ within density functional theory for a volatile liquid at gas–liquid coexistence shows, in comparison with this more complete theory the interface displacement model misses a contribution which is independent of the shape $l(x)$ and is determined by θ_∞ and l_0 (the first term in the sum in Eq. (2.19) in Ref. [34], denoted as $\tilde{\tau}$ in Eqs. (4.2), (4.3), and (4.5) in Ref. [33]). Since, however, this constant contribution turns out to be numerically much smaller than those contributions captured by the interface displacement model (see Fig. 15 in Ref. [33]), we have refrained from determining it for the present, much more complicated geometry, assuming that the size ratios of these types of contributions remain roughly the same for the planar and the cylindrical substrate.

Figure 10 shows the dependence of the line tension τ on the cylinder radius R using the planar effective interface potential $\omega_p(l)$. τ is given by $s\sigma$ times a numerical factor on the order of 1. It decreases monotonously for decreasing R and attains its maximum value τ_∞ for $R \to \infty$ as $\tau_\infty - \tau(R) \sim R^{-1}$. We note that this decrease of the line tension upon decreasing the radius of curvature R of the contact line is opposite to the increase of the effective line tension $\tau_{eff}(z_1)$ observed for a decreasing radius of curvature z_1 of the circular three-phase contact line on a planar substrate as can be
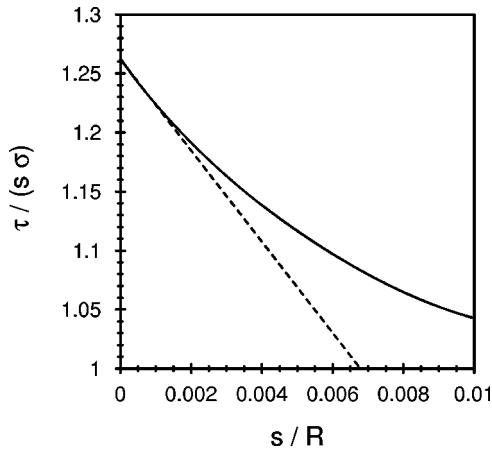
FIG. 10. Dependence of the line tension τ (full curve) of macroscopic ''barrel''-type drops ($\kappa=0$) on cylinders of radius R. The corresponding interface profiles and apparent contact angles are shown in Figs. 8 and 9, respectively. τ is calculated by using the planar effective interface potential $\omega_p(l)$. As indicated by the dashed line, τ approaches τ_∞ for $R\rightarrow\infty$ as $\tau_\infty - \tau \sim R^{-1}$. τ_∞ is the line tension of the straight three-phase contact line on the corresponding planar substrate.

inferred from Fig. 9(b). Thus line tensions of curved three-phase contact lines can be smaller or larger than the line tension of the corresponding straight contact lines.

Whereas τ_∞ is experimentally accessible by monitoring the apparent contact angle of sessile droplets on a planar substrate as a function of the droplet size, $\tau(R)$ cannot be determined experimentally by direct observation. The basic reason for this difference is that the length $2\pi z_1$ of the three-phase contact line of the sessile drop on the planar substrate can vary as a function of the droplet size so that the optimal shape of the droplet responds to the associated cost $2\pi z_1 \tau_\infty$ of the free energy, whereas the excess free energy $2\pi R \tau(R)$ for the ends of the droplets is a constant contribution with respect to the droplet size on the cylinder due to the fixed value of R. This, however, holds only for the ''barrel''-type shape of the drop, for which the length of the three-phase contact lines is fixed. For ''clamshell''-type droplet shapes the length of the three-phase contact line does depend on the droplet size so that in this case the line tension will influence the droplet shape. Nonetheless there are systems for which $\tau(R)$ can be experimentally relevant. If the cylinder is not a hard solid rod but consists of a soft material like, e.g., vesicles or tobacco viruses, which float vertically at the liquid–vapor interface of a solvent, the positive line tension $\tau(R)$ will strangle the object locally, depending on its restoring elastic forces. According to Fig. 10 this tweaking force $-d[\tau(R)R]/dR$ is weaker for thin cylinders.

V. SUMMARY

Based on an interface displacement model [Eq. (2.5)] we have analyzed the shape and the free energy of ''barrel''-type droplets of fixed volume V_{ex} covering a cylindrical substrate of radius R (Fig. 1). For sufficiently small droplets their shape $h(z)=R+l(z)$ is not only governed by the surface tension σ of the liquid–vapor interface but also by the effective interface potential $\omega_c(l;R)$ with a generic form as shown in Fig. 2. We have obtained the following main results:

(1) Figures 3 and 4 show how the deviation of the actual droplet shape $h(z)$ from a suitably defined reference configuration $a_{ref}(z)$ depends on the droplet size. The reference configuration is uniquely defined by the requirement to touch the actual shape at the apex and to have a constant mean curvature which equals the actual one at the apex. $a_{ref}(z)$ allows one to introduce an apparent contact angle θ, characterizing the actual shape, which can be expressed in terms of the experimentally accessible quantities cylinder radius R, radii of curvature at the apex, height $l(0)$ of the droplet, and thickness l_0 of the wetting layer outside the barrel [Eq. (2.4)].

(2) The dependence of the effective interface potential $\omega_c(l;R)$ on the cylinder radius R influences the shape of the droplet on the scale of the range s of $\omega_c(l;R)$ (Fig. 5); this dependence has a rather marked effect on the apparent contact angle (Fig. 7).

(3) The apparent contact angles increase for smaller droplets and for thicker cylinders (Fig. 6). The contact angles of macroscopically large drops approach the Young's contact angle on a planar substrate proportional to $1/R$ [Fig. 9(a)].

(4) In the limiting case of small droplets on a planar substrate the circular bend of the three-phase contact line leads to an effectively increased value of the corresponding line tension [Fig. 9(b)]. This deviation from the Neumann–Boruvka equation becomes relevant if the droplet radius is less than roughly 500 nm. This observation is relevant for experimental determinations of line tensions via contact angle measurements.

(5) For macroscopically large drops their shape $l(z)$ increases linearly on a planar substrate but exponentially on a cylinder [Fig. 1(b)]. Figure 8 illustrates the smooth crossover between these types of behavior for increasing cylinder radii.

(6) For large cylinder radii the line tension associated with the ends of macroscopically large drops approaches the line tension of three-phase contact on a planar substrate proportional to $1/R$ (Fig. 10).

[1] B.J. Carroll, J. Colloid Interface Sci. **97**, 195 (1984).

[2] B.J. Carroll, Langmuir **2**, 248 (1986).

[3] B.J. Carroll, in *Contact Angle, Wettability and Adhesion*, edited by K.L. Mittal (VSP, Utrecht, 1993), p. 235; J. Appl. Phys. **70**, 493 (1991).

[4] P. Levinson, J. Jouffroy, and F. Brochard, J. Phys. (France)

Lett. **46**, L21 (1985); F. Brochard, J. Chem. Phys. **84**, 4664 (1986).

[5] D. Quéré, J.-M. di Meglio, and F. Brochard-Wyart, Rev. Phys. Appl. **23**, 1023 (1988); Europhys. Lett. **10**, 335 (1989); Science **249**, 1256 (1990), and references therein; A. de Ryck and D. Quéré, C. R. Acad. Sci., Ser. II: Mec., Phys., Chim., Sci.

Terre Univers **316**, 1045 (1993); **317**, 891 (1993); V.I. Ivanov, D. Quéré, J.-M. di Meglio, and V.M. Starov, *Colloid J. Russian Acad. Sci.* **54**, 346 (1992); D. Quéré and J.-M. di Meglio, Adv. Colloid Interface Sci. **48**, 141 (1994).

[6] S. Rooks, L.M. Racz, J. Szekely, B. Benhabib, and A.W. Neumann, Langmuir **7**, 3222 (1991).

[7] H.D. Wagner, J. Appl. Phys. **67**, 1352 (1990); **70**, 495 (1991).

[8] A.L. Yarin, A. Oron, and P. Rosenau, Phys. Fluids A **5**, 91 (1993).

[9] Y.-N. Lee and S.-M. Chiao, J. Colloid Interface Sci. **181**, 378 (1996).

[10] M. Connor, P.H. Harding, J.-A.E. Månson, and J.C. Berg, J. Adhes. Sci. Technol. **9**, 983 (1995).

[11] G. McHale, N.A. Käb, M.I. Newton, and S.M. Rowan, J. Colloid Interface Sci. **186**, 453 (1997); G. McHale, S.M. Rowan, M.I. Newton, and N.A. Käb, J. Adhes. Sci. Technol. **13**, 1457 (1999).

[12] J.R. de Bruyn, Phys. Fluids **9**, 1599 (1997).

[13] B. Song, A. Bismarck, R. Tahhan, and J. Springer, J. Colloid Interface Sci. **197**, 68 (1998).

[14] Y. Gu and D. Li, J. Colloid Interface Sci. **206**, 288 (1998).

[15] L.M. Jenkins and A.M. Donald, Langmuir **15**, 7829 (1999).

[16] E. Dujardin, T.W. Ebbesen, A. Krishnan, and M.M.J. Treacy, Adv. Mater. **10**, 1472 (1998).

[17] P.M. Ajayan, O. Stephan, P. Redlich, and C. Collex, Nature (London) **375**, 564 (1995).

[18] T.W. Ebbesen, H. Hiura, M.E. Bisher, M.M.J. Treacy, J.L. Shreeve-Keyer, and R.C. Haushalter, Adv. Mater. **8**, 155 (1996).

[19] E. Dujardin, T.W. Ebbesen, H. Hiura, and K. Tanigaki, Science **265**, 1850 (1994).

[20] T. Kasuga, M. Hiramatsu, A. Hoson, T. Sekino, and K. Nii-hara, Langmuir **14**, 3160 (1998).

[21] P. Kim and C.M. Lieber, Science **286**, 2148 (1999).

[22] S. Dietrich, in *Phase Transitions and Critical Phenomena*, edited by C. Domb and J.L. Lebowitz (Academic, London, 1988), Vol. 12, p. 1.

[23] A. Neimark, J. Adhes. Sci. Technol. **13**, 1137 (1999).

[24] J.Y. Wang, S. Betelu, and B.M. Law, Phys. Rev. Lett. **83**, 3677 (1999).

[25] K.R. Neumaier, G. Elender, E. Sackmann, and R. Merkel, Europhys. Lett. **49**, 14 (2000).

[26] F. Rieutord and M. Salmeron, J. Phys. Chem. B **102**, 3941 (1998).

[27] S. Herminghaus, A. Fery, and D. Reim, Ultramicroscopy **69**, 211 (1997); T. Pompe, A. Fery, and S. Herminghaus, Langmuir **14**, 2585 (1998); A. Fery, T. Pompe, and S. Herminghaus, J. Adhes. Sci. Technol. **13**, 1071 (1999); T. Pompe, A. Fery, and S. Herminghaus, *ibid.* **13**, 1155 (1999); T. Pompe and S. Herminghaus, Phys. Rev. Lett. (to be published).

[28] J.S. Rowlinson and B. Widom, *Molecular Theory of Capillarity* (Clarendon, Oxford, 1982).

[29] T. Bieker and S. Dietrich, Physica A **252**, 85 (1998); **259**, 466 (1998).

[30] J.O. Indekeu, Int. J. Mod. Phys. B **8**, 309 (1994).

[31] B.J. Carroll, J. Colloid Interface Sci. **57**, 488 (1976).

[32] J. Yamaki and Y. Katayama, J. Appl. Polym. Sci. **19**, 2897 (1975).

[33] T. Getta and S. Dietrich, Phys. Rev. E **57**, 655 (1998).

[34] C. Bauer and S. Dietrich, Eur. Phys. J. B **10**, 767 (1999).

[35] N.K. Adam, J. Soc. Dyers Colour. **53**, 122 (1937).

[36] L. Boruvka and A.W. Neumann, J. Phys. Chem. **66**, 5464 (1977).

[37] H. Dobbs, Int. J. Mod. Phys. B **13**, 3255 (1999).

[38] H.T. Dobbs and J.O. Indekeu, Physica A **201**, 457 (1993).